

Refining local-type primordial non-Gaussianity: Sharpened b_ϕ constraints through bias expansion

Boryana Hadzhiyska^{1,2,*} and Simone Ferraro^{1,2}

¹*Physics Division, Lawrence Berkeley National Laboratory, Berkeley, CA 94720, USA*

²*Berkeley Center for Cosmological Physics, Department of Physics,
University of California, Berkeley, CA 94720, USA*

Local-type primordial non-Gaussianity (PNG), predicted by many non-minimal models of inflation, creates a scale-dependent contribution to the power spectrum of large-scale structure (LSS) tracers. Its amplitude is characterized by the product $b_\phi f_{\text{NL}}^{\text{loc}}$, where b_ϕ is an astrophysical parameter dependent on the properties of the tracer. However, b_ϕ exhibits significant secondary dependence on halo concentration and other astrophysical properties, which may bias and weaken the constraints on $f_{\text{NL}}^{\text{loc}}$. In this work, we demonstrate that incorporating knowledge of the relation between Lagrangian bias parameters and b_ϕ can significantly enhance PNG constraints. We employ the Hybrid Effective Field Theory (HEFT) approach at the field-level and a linear regression model to seek a connection between the bias parameters and b_ϕ for halo and galaxy samples, constructed using the ABACUSSUMMIT simulation suite and mimicking the luminous red galaxies (LRGs) and quasi-stellar objects (QSOs) of the Dark Energy Spectroscopic Instrument (DESI) survey. For the fixed-mass halo samples, our full bias model reduces the uncertainty by more than 70%, with most of that improvement coming from b_∇ , which we find to be an excellent proxy for concentration. For the galaxy samples, our model reduces the uncertainty on b_ϕ by 80% for all tracers. By adopting Lagrangian-bias informed priors on the parameter b_ϕ , future analyses can thus constrain $f_{\text{NL}}^{\text{loc}}$ with less bias and smaller errors.

I. INTRODUCTION

Understanding the origins of cosmic structures requires the investigation of the nature of primordial density fluctuations. One of the most exciting prospects of this quest is finding non-Gaussian features imprinted during the earliest moments after the Big Bang, which would illuminate the physics of the high-energy regime and put constraints on the widely accepted paradigm of inflation [1]. Unraveling inflation would offer a unique path to probing the seeds of cosmic structure formation and allow us to delve deeper into the fundamental mechanisms of the Universe.

Among the various types of primordial non-Gaussianity (PNG), the most well-studied is the local-type PNG, which links the small-scale with the large-scale galaxy density distribution and is characterized by a parameter $f_{\text{NL}}^{\text{loc}}$. Local-type PNG holds significant promise for offering insights into the early universe, as a detection of $f_{\text{NL}}^{\text{loc}} \sim 1$ would provide compelling evidence for the existence of multiple fields during inflation, which makes it a critical target for current and future cosmological surveys [2, 3].

A number of analyses have tried to constrain the parameter $f_{\text{NL}}^{\text{loc}}$ both in the cosmic microwave background (CMB) [4] and in the large-scale structure (LSS) [5]. While the Planck satellite has provided stringent constraints on $f_{\text{NL}}^{\text{loc}}$, with $f_{\text{NL}}^{\text{loc}} = -0.9 \pm 5.1$ [6], future large-scale structure surveys are expected to significantly improve this sensitivity [7–13], and bring it well beyond

the forecasts for future CMB experiments [14, 15]. The key to these improvements lies in the larger number of Fourier modes available for 3D vs. 2D surveys and the scale-dependent bias effect induced by local-type PNG on the galaxy density field on large scales.

While theoretically exciting, there are still difficulties associated with observing the signal and interpreting it. For example, on large scales the effect of survey sample variance is extremely large. A particularly powerful approach for reducing this effect is multi-tracer analysis, which can potentially bring down the precision to $\sigma[f_{\text{NL}}^{\text{loc}}] < 1$ [12, 13, 16–23]. Additionally, to uncover these subtle non-Gaussian imprints, we need to disentangle astrophysical and non-linear evolution effects from the features of the primordial Universe. These non-cosmological effects are quantified by the bias parameter b_ϕ , which a number of previous analyses assume to be perfectly correlated with the linear tracer bias b_1 (or halo mass) [24–29].

Recent studies have highlighted that the assumed relationship between b_ϕ and the linear bias b_1 might be oversimplified, especially when secondary halo properties related to the merger history are considered [30, 31]. For this reason, some more recent works have instead reported constraints on the product $b_\phi f_{\text{NL}}^{\text{loc}}$ [28, 29, 32], which appears in the scale-dependent bias relation. This realization opens new avenues for constraining $f_{\text{NL}}^{\text{loc}}$ by refining the models that relate b_ϕ to observable properties of galaxies and halos because any uncertainty on b_ϕ automatically translates into uncertainty on $f_{\text{NL}}^{\text{loc}}$ as $\sigma[f_{\text{NL}}^{\text{loc}}] \propto \sigma[b_\phi]/b_\phi$. A promising approach involves the use of advanced simulations and bias expansion models to capture the complex dependencies of b_ϕ .

State-of-the-art numerical simulations have revolutionized our ability to explore the complex interplay between

* boryanah@berkeley.edu

primordial physics and LSS [e.g., 33–38]. These simulations provide an invaluable laboratory for studying the link between galaxy formation and primordial physics, which is crucial for disentangling $f_{\text{NL}}^{\text{loc}}$ from b_ϕ . Recent works have explored the relationship between b_ϕ and b_1 in simulations [30, 32, 39, 40] and found that beyond the simple linear (universality) relation, there is a significant secondary dependence of b_ϕ on halo formation history properties such as concentration [31, 41]. Unfortunately, most of these properties are not observable and instead a number of large-scale analyses only measure ‘bias parameters’ associated with a perturbative expansion model [42].

In this work, we demonstrate that incorporating a detailed understanding of tracer bias parameters into the estimation of b_ϕ can significantly enhance the precision of PNG constraints. This approach not only sheds light on the complex interplay between astrophysical quantities and cosmological perturbation theories, but also sets the stage for more accurate and robust measurements of the primordial fluctuations in the early Universe. In particular, we aim to refine the estimation of b_ϕ using a Lagrangian bias expansion model. This approach allows us to incorporate the influence of various bias parameters and halo properties on b_ϕ , thereby providing a more accurate and comprehensive understanding of the scale-dependent bias induced by local-type PNG. We utilize the suite of high-resolution N-body simulations, AbacusSummit, together with the ‘Separate Universe’ technique, which can be employed to understand the response of small-scale galaxy physics to long-wavelength fluctuations. Furthermore, we extend our study beyond halos to galaxies by utilizing an advanced halo occupation distribution (HOD) model to approximate the luminous red galaxies (LRGs) population targeted by the Dark Energy Spectroscopic Instrument (DESI) survey. We show that we are able to improve the uncertainty on b_ϕ and thus $f_{\text{NL}}^{\text{loc}}$ by more than 80% for all galaxy tracer samples considered in this study.

We begin Section II by introducing the AbacusSummit simulation suite, describing relevant halo properties and the Separate Universe technique, detailing the construction of galaxy samples that mimic the galaxy survey DESI, and reviewing the theoretical background of the Lagrangian bias model HEFT. In Section III, we analyze the dependence of b_ϕ on Lagrangian bias and concentration and present our forecasts for reducing the uncertainty on b_ϕ and thus $f_{\text{NL}}^{\text{loc}}$. Importantly, we perform a realistic study of the scatter of b_ϕ for galaxy samples and investigate the effect of adopting a simple linear model. Finally, we discuss the implications of our findings for future LSS surveys and summarize our conclusions in Section IV.

II. METHODS

A. AbacusSummit

ABACUSSUMMIT is a suite of cosmological N -body simulations designed to meet and exceed the Cosmological Simulation Requirements of the DESI survey [43]. The simulations were run with ABACUS [44, 45], a high-accuracy, high-performance cosmological N -body simulation code, optimized for GPU architectures and for large-volume simulations, on the Summit supercomputer at the Oak Ridge Leadership Computing Facility.

Here, we employ the `base` resolution boxes of ABACUSSUMMIT, each of which contains 6912^3 particles in a $2 h^{-1}\text{Gpc}$ box, each with a mass of $M_{\text{part}} = 2.1 \times 10^9 h^{-1}\text{M}_\odot$. While the ABACUSSUMMIT suite spans a wide range of cosmologies, here we focus on a single realization of the fiducial cosmology (*Planck* 2018: $\Omega_b h^2 = 0.02237$, $\Omega_c h^2 = 0.12$, $h = 0.6736$, $10^9 A_s = 2.0830$, $n_s = 0.9649$, $w_0 = -1$, $w_a = 0$), `AbacusSummit_c000_ph000` as well as two additional runs with a 2% higher and lower values of σ_8 , `AbacusSummit_c112_ph000` and `AbacusSummit_c113_ph000`. In particular, utilize the halo and particle catalogs [46] as well as initial conditions outputs. For full details on all data products, see Ref. [43].

B. Concentration definition

The link between halo concentration and accretion history has been studied extensively in the literature [47–50], and it has been shown that recent merger activity induces dramatic changes in the halo concentration, and that these responses linger over a period of several dynamical times, corresponding to many Gyr [see, e.g., 51]. Relevant to galaxy surveys is the fact that halo concentration has a bearing on both the halo occupation distribution and the galaxy clustering clustering [e.g., 49, 52–55], and recent evidence in data suggests that different galaxy samples have different host halo concentrations [56].

Similarly to Ref. [41], we adopt the following proxy for halo concentration:

$$c = r_{90}/r_{25}, \quad (1)$$

following the recommendation of Ref. [46], where r_{90} and r_{25} are defined as the radii, within which 90% and 25% of the halo particles are contained inside a sphere centered on the halo center. For more details on the halo finder and virial mass definition, we refer the reader to Ref. [57] and Ref. [46].

C. Local environment

The effect of environment on the halo and galaxy clustering has been studied extensively in the literature [58–

61]. A halo residing in a dense region is expected to contain more galaxies on average than a halo in an underdense region because halos in overdense regions experience more mergers, whereas those in underdense regions accrete mass more smoothly.

To define halo environment, we adopt the same formalism as Ref. [62]. Specifically, for each halo, we find all neighboring halos beyond its virial radius but within $r_{\max} = 5 h^{-1} \text{Mpc}$ of the halo center. We sum the mass of all neighboring halos, denoted by M_{env} , and define the environment parameter, f_{env} :

$$f_{\text{env}} = M_{\text{env}} / \bar{M}_{\text{env}} \quad (2)$$

where \bar{M}_{env} is the mean environment parameter within halo mass bin M .

D. Separate Universe approach

We employ the separate universe technique to measure the local-type PNG-induced bias, b_ϕ , by invoking the equivalence between the response of galaxy formation to long-wavelength perturbations and the response of galaxy formation to changes in the background cosmology. The separate universe argument states that as long as the physics of galaxy formation acts on much smaller scales compared with the size of the long-wavelength perturbations, these long-wavelength perturbations act as a modified background to the process of galaxy formation [this is known as the ‘peak-background split’ argument; see e.g., 63, 64]. Thus, the formation of galaxies at fixed cosmology in some region of space embedded in a long-wavelength fluctuation is equivalent to the formation of galaxies in a modified cosmology.

To access the quantity b_ϕ , the modified cosmology needs to have a different amplitude of the primordial scalar power spectrum, A_s , or equivalently, the amplitude of the linear power spectrum on the scale of $8 \text{ Mpc}/h$, i.e., σ_8 . Mathematically, the PNG-induced bias, b_ϕ , is defined as

$$f_{\text{NL}}^{\text{loc}} b_\phi \equiv \frac{d \ln n_h(z)}{d \phi}, \quad (3)$$

which can be expressed as:

$$b_\phi = 4 \frac{d \ln n_h(z)}{d A_s} = 2 \frac{d \ln n_h(z)}{d \sigma_8} \quad (4)$$

by noting that [5, 24]

$$\tilde{A}_s = A_s [1 + \delta A_s], \quad \text{with} \quad \delta A_s = 4 f_{\text{NL}}^{\text{loc}} \phi_L, \quad (5)$$

where ϕ_L is to be treated as a constant locally and denotes the amplitude of the long-wavelength potential perturbation. Thus, we can evaluate b_ϕ in a separate universe with a different value of A_s (σ_8). In practice, we typically generate simulations with the same initial seed as the fiducial box, but with an input power spectrum file

multiplied by $[1 + \delta \sigma_8^2]$. In observations, making this measurement directly is extremely challenging, but recent works have suggested a possible path forward that directly extracts the PNG signal from the galaxy density field [10].

Here, we employ the ‘Linear derivative’ ABACUS-SUMMIT boxes, `base_c112_ph000` and `base_c113_ph000`, which have the same initial seed as the fiducial simulation `base_c000_ph000`, but a different value of σ_8 : namely, $\sigma_8^{\text{high}} = 1.02 \times \sigma_8^{\text{fid}}$ and $\sigma_8^{\text{low}} = 0.98 \times \sigma_8^{\text{fid}}$, respectively. We estimate b_ϕ in the separate universe approach as

$$b_\phi(z) = \frac{b_\phi^{\text{high}}(z) + b_\phi^{\text{low}}(z)}{2}, \quad (6)$$

where

$$b_\phi^{\text{high}}(z) = \frac{2}{\delta \sigma_8^{\text{high}}} \left[\frac{n_h^{\text{high}}(z)}{n_h^{\text{fid}}(z)} - 1 \right], \quad (7)$$

$$b_\phi^{\text{low}}(z) = \frac{2}{\delta \sigma_8^{\text{low}}} \left[\frac{n_h^{\text{low}}(z)}{n_h^{\text{fid}}(z)} - 1 \right]. \quad (8)$$

where $n_h^{\text{fid}}(z)$, $n_h^{\text{high}}(z)$ and $n_h^{\text{low}}(z)$ is the mean number density of halos (galaxies) in the fiducial, high- and low- σ_8 simulations at some redshift z .

E. Hybrid Effective Field Theory

In this section, we summarize our approach for estimating the higher-order bias parameters, used to describe the connection between biased tracers such as galaxies and halos, and the underlying matter field in Lagrangian Perturbation Theory (LPT). For a review of perturbation theory, see Ref. [65–67].

In the Lagrangian picture, we work with infinitesimal fluid elements labeled by their initial (Lagrangian) positions \mathbf{q} . Their dynamics are encoded in a displacement vector $\Psi(\mathbf{q}, \eta)$, sourced by the gravitational potential and defined such that the Eulerian (comoving) positions \mathbf{x} of the fluid element at some conformal time η is $\mathbf{x}(\mathbf{q}, \eta) = \mathbf{q} + \Psi(\mathbf{q}, \eta)$ [68, 69]. The 3D distribution of cosmological observables such as the galaxy field is, in general, determined by complex small-scale astrophysical processes and their response to the large-scale matter distribution [66].

We can thus write the dependence of the galaxy field along its trajectory as an expansion to second order in the initial conditions adopting the Lagrangian framework [70–73]:

$$F(\mathbf{q}) = 1 + b_1 \delta_L(\mathbf{q}) + b_2 (\delta_L^2(\mathbf{q}) - \langle \delta_L^2 \rangle) + b_s (s_L^2(\mathbf{q}) - \langle s_L^2 \rangle) + b_\nabla \nabla^2 \delta_L(\mathbf{q}), \quad (9)$$

where b_1 , b_2 , b_s and b_∇ are free bias parameters and $s_L^2 = s_{ij} s^{ij}$ is the shear/tidal field, with $s_{ij} \equiv (\partial_i \partial_j / \partial^2 - \delta_{ij}/3) \delta_L$. Note that the functional $F(\mathbf{q})$ can only depend on scalar combinations of the density field and the tidal

field. Nonlocality effects are handled by performing a Taylor expansion of the δ_L field around \mathbf{q} . To lowest order, this calls for the inclusion of $\nabla^2\delta_L$. We note that on nonlocal scales, smaller than the scale of astrophysical processes, the Lagrangian approximation breaks down. The functional can then be advected to the real-space (Eulerian) position \mathbf{x} [74]:

$$1 + \delta_g(\mathbf{x}) = \int d^3\mathbf{q} F(\mathbf{q}) \delta^D(\mathbf{x} - \mathbf{q} - \Psi(\mathbf{q})) \quad (10)$$

Thus, the 21cm clustering signal contains a dynamics piece, Ψ , as well as a piece depending on the initial conditions, $F(\mathbf{q})$.

To estimate the bias parameters, b_i , of our model, we minimize the difference between the model and the observable, δ_g . Our result can be expressed through the stochastic field $\epsilon(\mathbf{k})$, which represents residuals after removing deterministic contributions from the model:

$$\epsilon(\mathbf{k}) = \delta_g(\mathbf{k}) - \delta_m(\mathbf{k}) - \sum_i b_i(\mathbf{k}) \mathcal{O}_i(\mathbf{k}), \quad (11)$$

We obtain the bias parameters by solving the least squares problem of minimizing the error power spectrum, which yields the following expression for the bias parameters:

$$\hat{b}_i(\mathbf{k}) = \langle \mathcal{O}_i \mathcal{O}_j \rangle^{-1}(\mathbf{k}) \langle \mathcal{O}_j(-\mathbf{k}) [\delta_g(\mathbf{k}) - \delta_m(\mathbf{k})] \rangle. \quad (12)$$

Here, we estimate the bias parameters up to some maximum wavenumber, k_{\max} , as follows:

$$\hat{b}_i = M_{ij}^{-1} A_j. \quad (13)$$

where A_j and M_{ij} are defined as

$$\begin{aligned} A_j &= \langle [\mathcal{O}_j(\mathbf{x})(\delta_g(\mathbf{x}) - \delta_m(\mathbf{x}))]_{k_{\max}} \rangle, \\ &= \int_{|\mathbf{k}| < k_{\max}} \frac{d^3k}{(2\pi)^3} \mathcal{O}_j(\mathbf{k}) [\delta_g - \delta_m]^*(\mathbf{k}), \end{aligned} \quad (14)$$

and

$$\begin{aligned} M_{ij} &= \langle [\mathcal{O}_i(\mathbf{x}) \mathcal{O}_j(\mathbf{x})]_{k_{\max}} \rangle, \\ &= \int_{k_{|\mathbf{k}| < k_{\max}}} \frac{d^3k}{(2\pi)^3} \mathcal{O}_i(\mathbf{k}) \mathcal{O}_j^*(\mathbf{k}). \end{aligned} \quad (15)$$

F. Halo Occupation Distribution

In this work, we use the same mock catalogs that were constructed in Ref. [41] based on fits to the LRG and QSO clustering with DESI 1% data [see 75, and Table 1 therein for the parameter values we adopt when creating our synthetic LRG and QSO catalogs]. For our fiducial galaxy catalogs, we adopt the best fit values of these fits at redshifts $z = 0.5$, $z = 0.8$, and $z = 1.4$ for the three samples shown here, using the ABACUSSUMMIT boxes to ensure consistency of the halo mass and HOD parameter

definitions. We then consider assembly bias extensions around these fiducial values, including both environment and concentration dependence.

DESI targets LRGs at $z \lesssim 1$, with a fairly constant number density between $0.4 < z < 0.8$ of approximately $5 \times 10^{-4} [\text{Mpc}/h]^{-3}$. QSOs (quasars), on the other hand, are the tracer choice for studying large-scale structures at high redshifts, with a roughly constant number density between $0.8 < z < 2.1$, at $2 \times 10^{-5} [\text{Mpc}/h]^{-3}$.

The vanilla HOD model for both LRGs and QSOs is given by the standard formalism of Ref. [76]:

$$\bar{n}_{\text{cent}}(M) = \frac{f_{\text{ic}}}{2} \text{erfc} \left[\frac{\log_{10}(M_{\text{cut}}/M)}{\sqrt{2}\sigma} \right], \quad (16)$$

$$\bar{n}_{\text{sat}}(M) = \left[\frac{M - \kappa M_{\text{cut}}}{M_1} \right]^\alpha \quad (17)$$

where we note that the LRG satellite occupations equation has a modification in the form of multiplication by $\bar{n}_{\text{cent}}(M)$. M_{cut} determines the minimum mass of a halo to host a central galaxy, M_1 sets the pivot scale of the power law of satellite occupation, σ controls the steepness of the transition from 0 to 1 in the number of central galaxies, α is the power law index on the number of satellite galaxies, κM_{cut} gives the minimum halo mass to host a satellite galaxy, f_{ic} , which is a downsampling factor controlling the overall number density of the mock galaxies.

In the vanilla model, the velocity of the central galaxy is taken as the average velocity of the so-called “L2” subhalo [see 46]. For the satellite galaxies, the velocities are inherited from random halo particles. The analysis of Ref. [77] also includes velocity bias, which is necessary for modeling redshift-space clustering on small scales [e.g. 78, 79]. In the AbacusHOD model, it is parametrized as:

- $\alpha_{\text{vel,c}}$ modulates the peculiar velocity of the central galaxy relative to the halo center along the line-of-sight (LOS):

$$v_{\text{cent,z}} = v_{\text{L2,z}} + \alpha_{\text{vel,c}} \delta v(\sigma_{\text{LoS}}), \quad (18)$$

where $v_{\text{L2,z}}$ denotes the LOS component of the central subhalo velocity, $\delta v(\sigma_{\text{LoS}})$ denotes the Gaussian scatter, and $\alpha_{\text{vel,c}}$ is the central velocity bias parameter.

- $\alpha_{\text{vel,s}}$ modulates how the satellite galaxy peculiar velocity deviates from that of its host particle:

$$v_{\text{sat,z}} = v_{\text{L2,z}} + \alpha_{\text{vel,s}} (v_{\text{p,z}} - v_{\text{L2,z}}), \quad (19)$$

where $v_{\text{p,z}}$ denotes the line-of-sight component of particle velocity, and $\alpha_{\text{vel,s}}$ is the satellite velocity bias parameter.

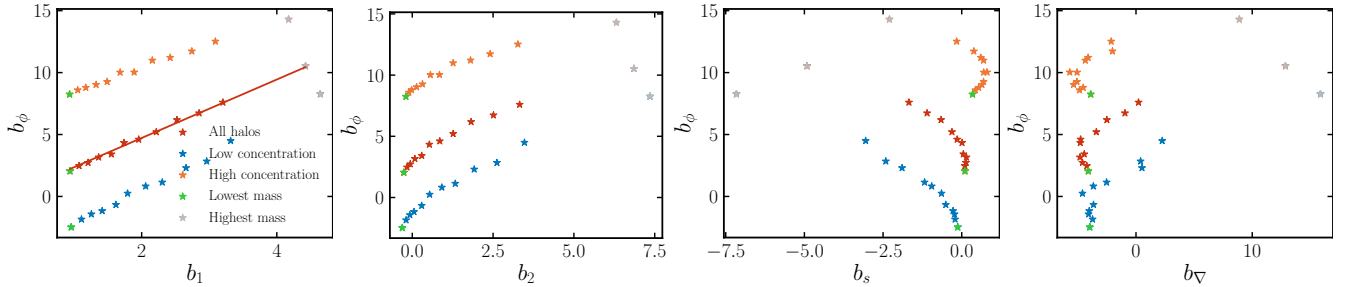


FIG. 1: Universality relations for all bias parameters as a function of halo mass and concentration, for halos at $z = 0.5$ split into 17 mass bins between 12.5 and 14.5 and three equally sized concentration bins. The effect of concentration is mostly captured as a variation in the p parameter (with $c = 0.7$, see Eq. 20). Similarly to b_1 , the relationship between b_2 and b_ϕ is almost exactly linear. b_s exhibits an opposite trait, where large values of b_s correspond to smaller values of b_ϕ . Small values of b_∇ and large values of b_s , which are typically measured for low-mass halos, map to a large range of b_ϕ , making that relationship less informative on its own.

III. RESULTS

The focal point of this paper is the study of the relationship between b_ϕ and the Lagrangian biases, b_X , as well as the assembly bias parameters such as concentration and environment. We do this for both galaxy and halo samples, though we note that in realistic surveys halos are not directly accessible. Nonetheless, halo samples provide key insights and indicate the power of future cluster-based analysis.

A. Halos

1. Universality relations and concentration

When performing PNG analysis, many works assume that the b_ϕ parameter is known exactly, and its value is extracted from the well-known universality relation, linking it to the linear bias parameter, b , as [5, 24]:

$$b_\phi = 2c\delta_c(b - p), \quad (20)$$

where in this work, we adopt $p = 1$, c ranges from 0.7 to 1, and $\delta_c = 1.686$. Note that the connection between linear bias and the Lagrangian bias, b_1 , is given by $b = 1 + b_1$.

However, as exemplified by a number of recent works, the scatter between b_ϕ and b_1 is non-trivial and non-negligible, since b_ϕ exhibits strong dependence on various astrophysical properties of the sample. One of the well-known properties in the case of halos is concentration. Additionally, the other bias parameters, b_2 , b_s , and b_∇ , also encode astrophysical information and can thus help in pinpointing the value of b_ϕ better and reducing the scatter. First, we explore the universality relations for all bias parameters as a function of halo mass and concentration in Fig.

We split the halos at $z = 0.5$ into 17 mass bins between 12.5 and 14.5. At each mass bin, we split the halos into three equally sized concentration bins and compute the

value of b_ϕ as well as the additional bias parameters, b_1 , b_2 , b_s and b_∇ , for each case. The relation between b_1 and b_ϕ follows the universality relation very closely, as expected. The effect of concentration is mostly captured as a variation in the p parameter (see Eq. 20), with the high-concentration halos exhibiting larger values of b_ϕ compared with the low-concentration ones. Similarly to b_1 , the relationship between b_2 and b_ϕ is almost exactly linear, with concentration modulating that relation by a constant positive or negative offset to b_ϕ , but with no significant shift to b_2 . b_s exhibits an opposite trait, where large values of b_s correspond to smaller values of b_ϕ . In addition, we see that the value of b_s at small halo mass (i.e. large b_s) seems to be very stable. In other words, given a measurement of b_s close to zero for some halo sample, one would not be able to pinpoint very well what the value of b_ϕ is for those halos. Similarly, small values at b_∇ , which are typically measured for low-mass halos, map to a large range of b_ϕ , making that relationship less informative, provided that only $b_\nabla \approx -5$ is measured for a given halo sample.

However, in practice we typically know the halo mass or equivalently linear bias fairly well for a given halo (or galaxy) sample. Thus, a more interesting question is whether measuring these additional bias parameters can help us reduce the scatter at fixed halo mass. We reiterate that while these universality relations give us an idea of the behavior of these halos on average at some fixed mass, they do not capture deviations due to selection effects such as concentration assembly bias. To better understand how well we can characterize the scatter around the mean values of b_ϕ at fixed halo mass, we study the correlation between b_ϕ and the 4 bias parameters at fixed halo mass.

2. Correlation between bias parameters

We show this in Fig. 2 for two halo masses, $\log M_h = 13.3, 13.8$, which are of interest to current and future

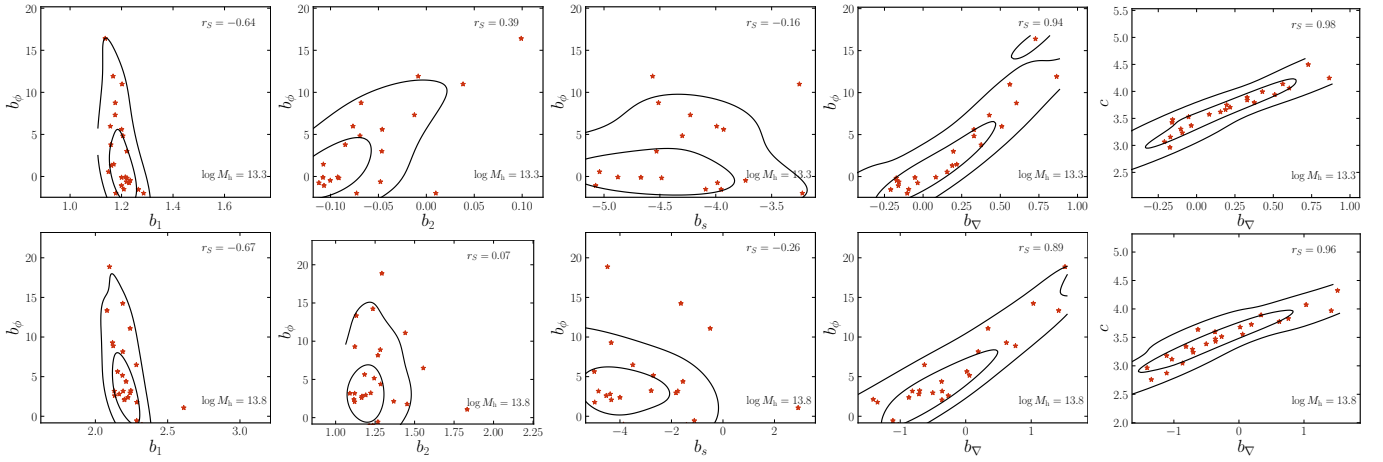


FIG. 2: Correlation between b_ϕ and the 4 bias parameters at fixed halo mass, shown for two halo masses, $\log M_h = 13.3, 13.8$, with contours indicating 68% and 95% percentile. A high Spearman correlation coefficient, r_s , means that if we know well the mass of the halo sample and the value of that parameter, we can pinpoint b_ϕ with a small amount of uncertainty. Looking at these plots, we see that consistently b_1 and b_∇ appear to be more highly correlated with b_ϕ . We also find that concentration and b_∇ are very strongly correlated – with Spearman coefficients around 0.95 for the mass range of interest. In other words, if one knows the concentration or more practically b_∇ for a given halo tracer, then identifying b_ϕ can be done with a small error bar. We note that in practice we rarely work directly with the halo field and often b_∇ absorbs counterterms as well as baryonic and astrophysical non-local effects.

surveys, with the contours indicating 68% and 95% percentile. The insight we get from studying these two mass bins is qualitatively similar to other mass bins, so we opt to only show those two. In each panel, we indicate the Spearman correlation, r_s coefficient between the two parameters with positive values indicating a positive correlation and vice versa. Values of r_s close to zero correspond to no correlation and $|r_s| = 1$ is maximal correlation. A high Spearman correlation coefficient between b_ϕ and some bias parameter b_X means that if we know well the mass of the halo sample and the value of that parameter, we can pinpoint b_ϕ with a small amount of uncertainty. Looking at these plots, we see that consistently b_1 and b_∇ appear to be more highly correlated with b_ϕ (though in the case of b_1 it is only $\sim 65\%$): in fact, the correlation between b_∇ and b_ϕ is so high that at fixed mass knowing one implies knowing the other with a high level of certainty. If one has direct access to a halo catalog, this is a very interesting and encouraging result.

To track down where this dependence arises from, we also study the correlation between concentration and b_∇ as the last panel in Fig. 2. Given the strong response of b_ϕ to both b_∇ and concentration, we find that concentration and b_∇ are very strongly correlated – with Spearman coefficients around 0.95 for the mass range of interest. To our knowledge, this tight correlation between concentration and b_∇ has not been pointed out previously. The connection between the two can be gleaned from the physical interpretation of b_∇ as the parameter specifying the response of the halo field to the curvature of the matter field. In other words, if one knows the concentration or more practically b_∇ for a given halo tracer, then identifying b_ϕ can be done with a small error bar. We

note that in practice we rarely work directly with the halo field and often b_∇ absorbs counterterms as well as baryonic and astrophysical non-local effects.

3. Reducing the uncertainty

We study by how much we can reduce the uncertainty of b_ϕ for the different halo mass bins next. Intuitively, we are trying to find what bias parameter or combination of bias parameters can capture best the scatter around the mean b_ϕ at fixed halo mass. While concentration is not a perfect proxy of b_ϕ , it does correlate strongly with it, and varying it does allow us to cover the full range of b_ϕ values that a given halo sample can take. For this reason, we split the halos in each mass bin into 25 concentration bins and measure the bias parameters, b_1, b_2, b_s, b_∇ , and b_ϕ , for each mass-concentration bin¹. Thus, assuming that the mass of the halo sample is known well, we proceed to fit b_ϕ as a function of the Lagrangian bias parameters for each mass bin. Specifically, we look for the linear coefficients, β , multiplying the biases that minimize the error on b_ϕ , i.e.

$$Y = \beta X, \quad (21)$$

where $Y^i = b_\phi^i$ and $X^i = [1, b_1^i, b_2^i, b_s^i, b_\nabla^i]$, with i running from 0 to $N_{\text{conc}} - 1 = 24$. The solution to this equation

¹ The goal of the mass-concentration binning is simply to capture the full range of values b_ϕ can take and look for trends with the Lagrangian bias parameters.

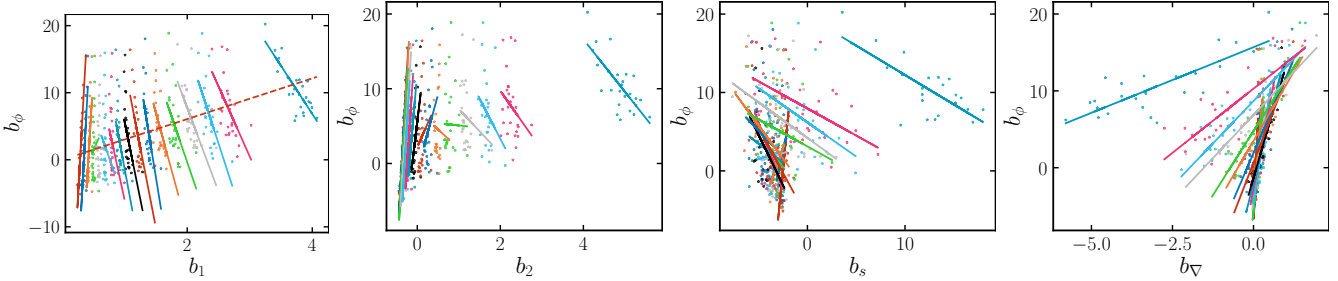


FIG. 3: Scatter plot of the values of the Lagrangian bias parameters and b_ϕ , where we have split the halos into 17 mass bins and 25 concentration bins. Halos belonging to the same mass bin are demarcated with the same color. The colored lines show the best-fit solution in the case of a single-parameter model, i.e. $b_\phi = \beta_0 + \beta_X b_X$, where X stands for one of the four Lagrangian bias parameters. For the higher-mass bin, the scatter in b_X for all four parameters is very large and thus, measuring b_X (in addition to the halo mass) yields an accurate estimate of b_ϕ , as can be seen in Table I, where for the highest-mass bin, all four single-parameter models lead to a large reduction on the uncertainty of b_ϕ .

is:

$$\beta = (X^T X)^{-1} X^T Y, \quad (22)$$

and we note that β_0 here is the Y offset. Technically, each entry i should be weighted differently to reflect the concentration-based sampling of b_ϕ , which is not necessarily properly weighting the different regions of b_ϕ space. However, we have tested that assigning coherently perturbed weights does not substantially alter our results.

Our metric for how well we capture the scatter is as follows: at fixed halo mass, we can calculate the uncertainty on b_ϕ as $\text{Std}[b_\phi^{\text{data}}]$. This is the price we need to pay on our uncertainty on $f_{\text{NL}}^{\text{loc}}$, since

$$\frac{\sigma[f_{\text{NL}}^{\text{loc}}]}{|f_{\text{NL}}^{\text{loc}}|} \propto \frac{\sigma[b_\phi]}{b_\phi}. \quad (23)$$

We would now like our model, $b_\phi^{\text{model}} \equiv \beta X$, to be as close as possible to b_ϕ^{data} , i.e. we want to minimize the scatter in $\Delta b_\phi \equiv b_\phi^{\text{data}} - b_\phi^{\text{model}}$ (this is in fact the solution we find in Eq. 22). We can quantify how well we have done through an improvement percentage, quantified as:

$$I[\%] \equiv 100 \times \left(1 - \frac{\text{Std}[\Delta b_\phi]}{\text{Std}[b_\phi^{\text{data}}]} \right). \quad (24)$$

We will focus on two types of models: those in which we make a fit with all Lagrangian parameters present, and those in which we only fit b_ϕ with one of the Lagrangian parameters at a time. These results are shown in Fig. 3 and Table I at $z = 0.5$. Our findings are qualitatively similar for other redshifts.

In Fig. 3, we show a scatter plot of the values of the Lagrangian bias parameters and b_ϕ , where each point corresponds to a concentration-mass bin (we split the halos into 17 mass bins and 25 concentration bins). Halos belonging to the same mass bin are demarcated with the same color, as our analysis assumes that we are working with a halo sample at fixed halo mass (e.g. identified through a cluster finding algorithm). The colored

lines show the best-fit solution in the case of a single-parameter model, i.e. $b_\phi = \beta_0 + \beta_X b_X$, where X stands for one of the four Lagrangian bias parameters. The intuition in case of the single-parameter model is as follows: in cases where the scatter of the points is small in b_X , we are not able to pinpoint the value of b_ϕ well, as knowing b_X does not give us any additional information. As an example, we see that for the higher-mass bin, the scatter in b_X for all four parameters is very large and thus, measuring b_X (in addition to the halo mass) yields an accurate estimate of b_ϕ , as can be seen in Table I, where for the highest-mass bin, all four single-parameter models lead to a large reduction on the uncertainty of b_ϕ .

Similarly, on the small-mass end, we see from the table that the performance of the b_1 and b_2 single-parameter models is very high, with the b_2 one being able to account for $\sim 70\%$ of the scatter. Looking at Fig. 3, we see that the variation of b_1 and b_2 is small for these low-mass samples, but it is very tight. Specifically, it appears that the scatter points b_1 - b_ϕ and b_2 - b_ϕ form a very thin straight line that is well captured by a single linear relationship. So for these very low-mass halos, $\log M_h \lesssim 13$, if the mass and b_2 are known (notice that b_2 performs better than b_1), then b_ϕ can be predicted with a high accuracy. A number of current and future surveys, however, will focus on the higher-mass regime, $\log M_h \gtrsim 13$. In this mass range, we see that the single-parameter model that provides the best results is the one based on b_∇ , which routinely explains well above 60% of the b_ϕ uncertainty. We link this to our previous finding from Fig. 2 that b_∇ is an excellent proxy for concentration and as a result tightly correlated with b_ϕ .

In theory, using all bias parameters ought to always yield the best performance, surpassing or doing as well as fewer-parameter models, as it is able to define a hyperplane that describes the data more accurately. This is indeed what we see in the table: the full-parameter model always does better than any of the single-parameter models. Specifically, for the halo masses most relevant for

Halo mass	All b 's	Only b_1	Only b_2	Only b_s	Only b_∇
$\log M_h = 12.6$	76.0%	61.6%	74.3%	21.9%	31.4%
$\log M_h = 12.7$	74.4%	37.4%	70.5%	4.3%	30.6%
$\log M_h = 12.8$	79.6%	21.8%	73.3%	2.9%	37.7%
$\log M_h = 12.9$	70.7%	0.4%	54.2%	0.6%	40.5%
$\log M_h = 13.0$	75.4%	0.0%	59.1%	0.1%	43.3%
$\log M_h = 13.1$	68.1%	1.7%	42.5%	0.1%	54.8%
$\log M_h = 13.2$	73.4%	7.2%	33.3%	12.7%	67.7%
$\log M_h = 13.3$	79.8%	14.8%	19.4%	1.3%	59.7%
$\log M_h = 13.4$	76.4%	16.0%	15.7%	10.0%	70.6%
$\log M_h = 13.5$	79.8%	27.3%	1.3%	13.3%	69.0%
$\log M_h = 13.6$	70.9%	26.6%	4.7%	2.5%	60.0%
$\log M_h = 13.7$	75.8%	23.6%	0.4%	15.7%	70.7%
$\log M_h = 13.8$	71.6%	13.2%	0.0%	3.4%	55.8%
$\log M_h = 13.9$	66.4%	24.7%	2.0%	14.4%	56.4%
$\log M_h = 14.0$	58.1%	22.8%	4.3%	9.4%	51.1%
$\log M_h = 14.1$	45.9%	18.6%	4.1%	11.1%	39.5%
$\log M_h = 14.8$	47.2%	41.2%	32.5%	34.9%	40.2%
All halos	35.3%	10.1%	10.6%	2.6%	0.1%

TABLE I: At small halo masses, the performance of the b_1 and b_2 single-parameter models is very high, with the b_2 one being able to account for $\sim 70\%$ of the scatter. In the higher mass range, relevant to current surveys, we see that the single-parameter model that provides the best results is the one based on b_∇ , which routinely explains well above 60% of the b_ϕ uncertainty. The full-parameter model always does better than any of the single-parameter models. Specifically, for the halo masses most relevant for large-scale surveys, i.e. $\log M_h$ between 13 and 14, the reduction of uncertainty on b_ϕ and hence f_{NL}^{loc} is around 75%. While we are interested in studying the performance of this model at fixed halo mass, we also show the result for all halos for completeness, in the last line of Table I. The reduction in uncertainty is only 35% in the full model and none of the single-parameter models can explain more than 10% of that uncertainty on its own.

large-scale surveys, i.e. $\log M_h$ between 13 and 14, the reduction of uncertainty on b_ϕ and hence f_{NL}^{loc} is around 75%. While we are interested in studying the performance of this model at fixed halo mass, we also show the result for all halos for completeness, in the last line of Table I. Interestingly, the reduction in uncertainty is only 35% in the full model and none of the single-parameter models can explain more than 10% of that uncertainty on its own. We surmise that this is the result of mixing

Tracer, redshift	All b 's	Only b_1	Only b_2	Only b_s	Only b_∇
LRG, $z = 0.5$	81.6%	13.1%	22.3%	2.7%	2.8%
LRG, $z = 0.8$	82.7%	10.7%	17.9%	1.9%	2.2%
QSO, $z = 1.4$	81.8%	4.9%	6.8%	0.0%	1.2%

TABLE II: Improvement percentages for the three tracer samples. While none of the single-parameter models reduces the scatter on b_ϕ by more than $\sim 20\%$ for the LRGs and $\sim 7\%$ for the QSOs, when combined together, the scatter is reduced by over $\gtrsim 80\%$ for all three tracers.

halo samples that have different responses to b_ϕ and the Lagrangian bias parameters. In addition, not imposing a fixed halo mass introduces degeneracies between the Lagrangian bias parameters and halo mass.

B. Galaxies

1. Constructing fair galaxy samples

Most potent for the search of PNG are large-volume spectroscopic surveys such as DESI, which aims to place $\sigma[f_{NL}^{loc}] \approx 5$ bounds through the auto-correlation analysis of its quasar (QSO) sample and its luminous red galaxy (LRG) samples. Here, we study all three samples in the cubic box at fixed redshift snapshots: LRG at $z = 0.5$, LRG at $z = 0.8$, and QSO at $z = 1.4$, constructed via the AbacusHOD model (see Section IIF). We do not adjust our analysis to the volume of the survey, as the goal of our exploration is to understand the connection between b_ϕ and the Lagrangian bias parameters b_X with minimal noise. We find that using a single simulation box, `AbacusSummit_base_c000_ph000` along with the field-level bias measuring technique (see Section IIE) and the Separate Universe approach (see Section IID) is sufficient for our purposes.

We have already learned that the halo properties that have a strong dependence on the value of b_ϕ are the halo mass and assembly bias parameters such as concentration and environment. For this reason, in designing the galaxy samples for this study, we adopted the best-fit parameters of the extended HOD analysis of Ref. [75], exploring modifications to six of the model parameters, namely: $\log M_{cut}$, $\log M_1$, the two main parameters controlling the halo masses entering the sample, A_c , A_s , the concentration assembly bias parameters, and B_c , B_s , the environment assembly bias parameters. Specifically, we vary the mass parameters within 0.2 dex of their best-fit values, the concentration ones between -2 and 2, and the environment ones between -0.5 and 0.5. We note that some of these variations appear to be ruled out by the tight constraints placed on the data, but at the same

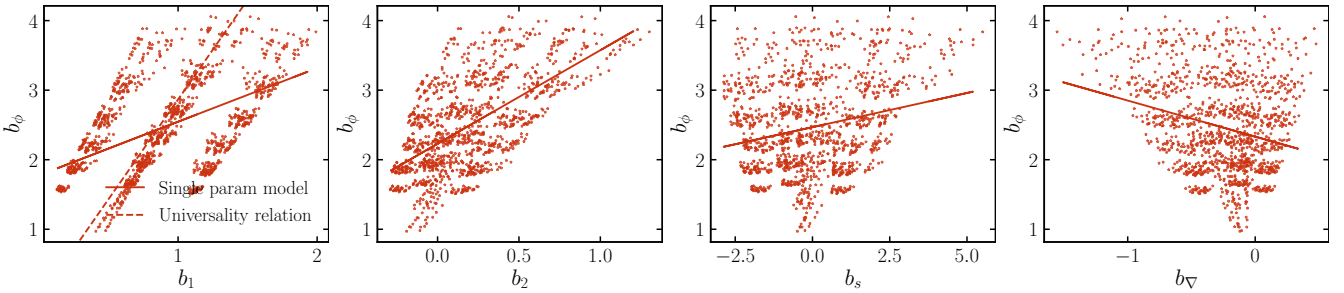


FIG. 4: Scatter plots of the b_X - b_ϕ plane for the LRGs at $z = 0.5$. The three islands visible in the first panel, b_1 - b_ϕ , correspond to the low, mid and high-environmental assembly biases cases from left to right, respectively. Single values of b_1 can correspond to a large range of possibilities for the environmental assembly bias parameter. The dashed line demarcates the universality relation between b_1 and b_ϕ for each tracer (with $c = 0.85$, see Eq. 20), which passes right through the no environmental assembly bias island in all cases. The solid line, as in the case of Fig. 3, shows the best-fit single-parameter model, $b_\phi = \beta_0 + \beta b_X$ for each of the four Lagrangian bias parameters.

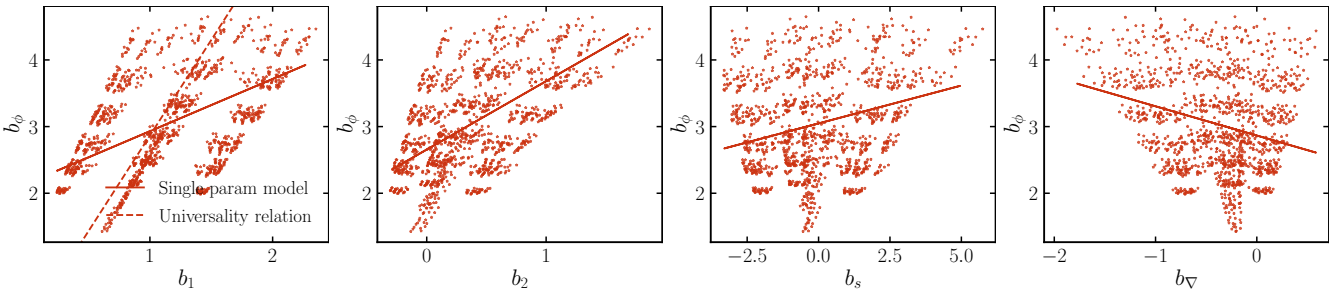


FIG. 5: As Fig. 4, but for the second LRG sample at $z = 0.8$. The two LRG samples appear to be qualitatively very similar with only small differences: at $z = 0.8$, it seems like all bias parameters cover a slightly broader range of values compared with the LRGs at $z = 0.5$.

time, assembly bias ornate-ments are currently not too well constrained.

We show scatter plots of the b_X - b_ϕ plane for the three galaxy tracer samples in Fig. 4, 5, and 6. As expected, the range of variation for both b_ϕ and the b_X parameters is more narrow compared with the halos, but the scatter still appears to be large. We note that the three islands visible in the first panel, b_1 - b_ϕ , for all three samples, correspond to the low, mid and high-environmental assembly biases cases from left to right, respectively. As noted previously, unlike concentration, environment leads to shifts in the x axis (rather than the y axis) [see e.g., 41]. We see that single values of b_1 can correspond to a large range of possibilities for the environmental assembly bias parameter. This accounts for the largest uncertainty on b_ϕ that we see in the samples we have defined.

2. Reducing the uncertainty

Unlike the halo case where we adopted fixed-mass samples, in the case of galaxies we are mixing very different halo masses and very different concentrations, which erases a lot of the information that turned out to be helpful in pinpointing the value of b_ϕ for halos. In addition, the presence of satellites and stochastic sam-

pling makes the connection between concentration and b_∇ more complex compared with the halo case. In practice, we know that concentration assembly bias does affect the galaxy occupation distribution in non-trivial ways: high-concentration halos are more likely to host centrals, whereas low-concentration halos are more likely to host satellites [see e.g., 80]. We do hope that the mix of halo masses and properties of the galaxy host halos can be disentangled by measuring a few of the Lagrangian bias parameters simultaneously. This is demonstrated in this section for the three galaxy samples of interest: LRGs at $z = 0.5$ and 0.8 and QSOs at $z = 1.4$.

As before, we fit a linear regression model to the measured values of b_ϕ and b_X for each of the HOD samples of a given tracer sample, of the form $b_\phi = \beta_0 + \sum_X \beta_X b_X$, where X is one of four Lagrangian bias parameters: b_1 , b_2 , b_s , b_∇ . We also evaluate the improvement percentage (see Eq. 24) relative to the case where we do not try to model b_ϕ and instead adopt some best-guess value and an empirically derived uncertainty on it, $\text{Std}[b_\phi^{\text{data}}]$, and also relative to single-parameter models of the form $b_\phi = \beta_0 + \beta_X b_X$. We show the best-fit lines for the single-parameter case as solid lines in Figs. 4, 5, and 6. The b_1 - b_ϕ universality relation is drawn as a dashed line in the first panel. We see that it goes almost exactly through the center of the middle ‘island’, suggesting that if little

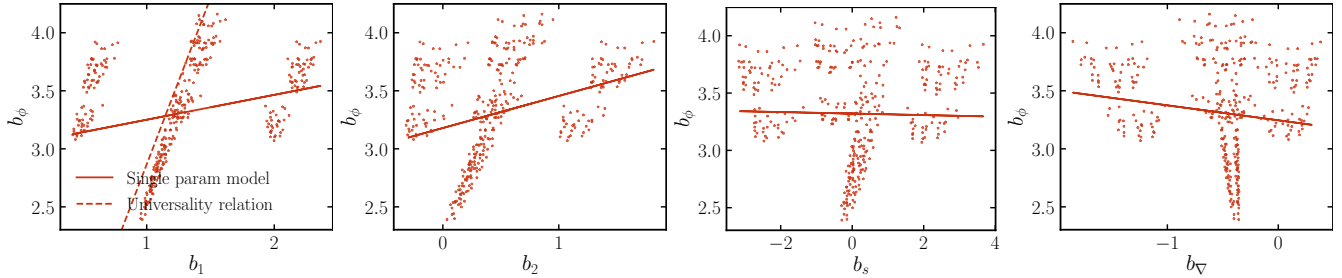


FIG. 6: As Fig. 4, but for the second QSO sample at $z = 1.4$. The three environment islands are more separated compared with the LRG samples. This is likely the case, as at higher redshifts and for more biased tracers, selecting halos with a large or small number of neighbors as done for large and small values of B_c and B_s pinpoints the environment of a halo. Thus, in this case, knowing b_1 can break the degeneracy with environmental assembly bias sufficiently well. In addition, we note that b_ϕ does not appear to vary as much compared with the LRG samples.

Tracer, redshift	β_0	b_1	b_2	b_s	b_∇	$\text{Std}[b_\phi^{\text{data}}]$	$\text{Std}[\Delta b_\phi]$
LRG, $z = 0.5$	1.18 ± 0.08	0.12 ± 0.08	4.87 ± 0.11	-0.98 ± 0.04	-1.03 ± 0.16	0.63	0.12
LRG, $z = 0.8$	1.74 ± 0.08	-0.30 ± 0.06	4.24 ± 0.07	-0.75 ± 0.04	0.09 ± 0.12	0.74	0.12
QSO, $z = 1.4$	3.38 ± 0.11	-0.54 ± 0.13	3.62 ± 0.16	-0.30 ± 0.02	2.01 ± 0.12	0.38	0.09

TABLE III: Best-fit values for the β coefficients multiplying the four bias parameters, b_X , and overall offset, β_0 . Using these along with the measured four bias parameters in a simple regression model allows us to predict b_ϕ and can serve as a prior in future PNG analysis. It is reassuring that the bestfit β coefficients for the two LRG samples are very similar, whereas the quasar sample yields slightly different values for the β 's.

or no assembly bias is present in the sample, it would provide a very good approximation to the value of b_ϕ . Visually, we see some stark similarities between the two LRG samples in terms of the relationship between the bias parameters and b_ϕ for the adopted HOD samples: similar trends to the mean b_X - b_ϕ relations, as well as the scatter of these relations. This consistency is reassuring in that it attests to the fact that we are observing true trends, as opposed to noise in the samples we have identified. While the QSO sample is different in some obvious ways (e.g., mean bias values and size of the scatter), we do find that the overall structure of the b_X - b_ϕ spaces is largely identical.

Looking at the improvement percentages in Table II, we see something surprising: while none of the single-parameter models reduces the scatter on b_ϕ by more than $\sim 20\%$ for the LRGs and $\sim 7\%$ for the QSOs, when combined together the scatter is reduced by over $\gtrsim 80\%$ for all three tracers. This shows that there is a hyperplane that connects b_ϕ and the Lagrangian bias parameters much more effectively than any of the b_ϕ - b_X cross-sections. Interestingly, out of the single-parameter models it is not the one based on b_1 or the one based on b_∇ , as the halo case would have led us to surmise, that gives the largest reduction on uncertainty, but instead it is the one based on b_2 . We explain this by noting that the mean halo mass for e.g. the LRG samples is around $\log M_h = 13.2$ and as can be seen from Table I, b_2 indeed is more tightly

correlated with b_1 for that mass scale. The reason b_∇ is no longer as effective at predicting b_ϕ is two-fold: we mix many mass scales in the galaxy sample now so the concentration- b_ϕ relationship is weakened; and in addition, b_∇ , which now absorbs a number of small-scale effects, is no longer tightly correlated with concentration.

3. Best-fit parameters

Ultimately, the goal of this work is to test the conjecture that pinpointing the Lagrangian bias parameters, which are measurable in a galaxy survey through e.g. the clustering statistics of a given galaxy sample, is beneficial to predicting b_ϕ , and thus $f_{\text{NL}}^{\text{loc}}$, with a smaller uncertainty. This seems to be manifestly true, as we are able to reduce the intrinsic scatter of b_ϕ , from 0.64, 0.70 and 0.41 to 0.11, 0.12, and 0.09, respectively, for the three tracers (see Table III), i.e. by about 80% (see Table II). For posterity, in Table III, we provide the best-fit model parameter values that lead to this substantial improvement, i.e. the values of β_0 and β_X , the coefficients multiplying the Lagrangian parameters, b_X .

The β coefficient values from this table along with the measured bias parameters b_X can be used jointly to predict b_ϕ and serve as prior for a PNG analysis. It is reassuring that the bestfit β coefficients for the two LRG samples are very similar, whereas the quasar sample yields

slightly different values for β . We note that these values are specific to analysis perform with the ABACUSSUMMIT suite and AbacusHOD prescription. In addition, when folding in our linear regression model into a PNG fit to real data, one would also need to marginalize over the error on these coefficients. Therefore, our recommendation is to perform the b_ϕ predictions on the fly with error bars when using ABACUSSUMMIT and otherwise, conduct a thorough recalibration of the fits.

IV. DISCUSSION AND CONCLUSIONS

Inferring the value of the cosmological parameter $f_{\text{NL}}^{\text{loc}}$ is crucial to understanding the origin of primordial fluctuations in the early Universe and ruling out or providing evidence for single-field inflationary models. Local-type PNG is usually investigated through the large-scale clustering properties of luminous tracers in cosmological surveys; however, to lowest order the quantity of interest, $f_{\text{NL}}^{\text{loc}}$, is fully degenerate with the bias parameter, b_ϕ , which characterizes the response of the particular tracer (e.g., galaxies, quasars) to changes in the fluctuations of the gravitational potential. While simplistic prescriptions such as the universality relation provide a link between linear bias and b_ϕ , recent works have demonstrated that different tracers will exhibit considerable deviations from the universality relation, depending on the assembly history and other astrophysical properties of the galaxy sample. Budgeting this uncertainty into the $f_{\text{NL}}^{\text{loc}}$ bounds is hefty, as $\sigma[f_{\text{NL}}^{\text{loc}}] \propto \sigma[b_\phi]/b_\phi$, so any vestigial uncertainty on b_ϕ is also present in the constraints on $f_{\text{NL}}^{\text{loc}}$. Additionally, adopting values for b_ϕ using the universality relation can also bias our inference on $f_{\text{NL}}^{\text{loc}}$ for certain tracers. For this reason, finding alternative ways of calculating b_ϕ is of great importance to future surveys. This is precisely the objective of this paper.

In this work, we show that measuring the second-order Lagrangian bias parameters, b_1 , b_2 , b_s , and b_∇ , in a galaxy survey is beneficial for predicting b_ϕ via a linear regression model, and thus, can be used for reducing the uncertainty on $f_{\text{NL}}^{\text{loc}}$. We summarize our main findings as follows:

- Through Fig. 1, we demonstrate that we can obtain a good fit to the mean halo bias- b_ϕ relation by adopting a simple modification to the universality relation (see Eq. 20). However, for samples preferentially featuring high- or low-concentration halos, we see a large variation in the b_1 - b_ϕ relation. The same holds true for the rest of the second-order Lagrangian bias parameters, which also exhibit their own universality relations with b_ϕ . These might be interesting to characterize in more detail in future works.
- We examine the bias- b_ϕ -concentration relation more closely for two representative halo mass bins in Fig. 2. Interestingly, we find that at fixed halo

mass, the correlation between b_ϕ and the parameter b_∇ is strongest (with correlation strength over 90%), followed by b_1 . We attribute this to the finding that for a fixed mass halo sample, b_∇ turns out to be an excellent proxy for halo concentration, which captures the majority of the intrinsic b_ϕ scatter.

- We follow up on this in Fig. 3 and Table I, where we perform fits to each of the fixed halo mass samples using a simple linear regression model between the four Lagrangian bias parameters, b_X , and b_ϕ . Visually, it is clear that there is a large amount of scatter in the values of b_ϕ ; however, we find that using even single-parameter models of the type $b_\phi = \beta_0 + b_X \beta_X$ can significantly reduce it. Which Lagrangian bias parameter to adopt in order to minimize the scatter depends on the mass of the halo sample: b_∇ yields a consistently large reduction, with b_1 and b_2 outperforming it only for small-mass halos. In all cases, the combined four-parameter model yields the best performance, allowing for more than 70% smaller uncertainty on b_ϕ .
- For maximum realism, we construct samples using the extended HOD model AbacusHOD (see Section II F). Specifically, we study the three most suitable DESI tracer samples for PNG searches due to their large volume and high bias: LRGs at $z = 0.5$ and $z = 0.8$ and QSOs at $z = 1.4$. We construct a large suite of HOD samples for each of the three tracer samples by varying two mass-related, two concentration-related and two environment-related HOD parameters. As these samples mix a large range of halo masses, the effect on b_ϕ from varying the concentration is much smaller compared with the halos, whereas the response to the environment assembly bias parameters is notable.
- Similarly to the halo samples, we study the reduction on the uncertainty of b_ϕ (and thus, indirectly, $f_{\text{NL}}^{\text{loc}}$) when adopting a linear regression model with each of the Lagrangian bias parameters and all of them together. We show these as scatter plots with best-fit lines in Fig. 4, 5, and 6. We quantify the mitigation of the scatter in all of these cases in Table II. Interestingly, we see that unlike the halo case, where some of the single-parameter models could significantly reduce the scatter, that is no longer the case for the galaxies, with the largest reduction being around 20%. However, surprisingly and encouragingly, the full-parameter models yield much larger improvements, of over 80% for all three tracers. We also provide the β coefficients from our linear regression model for each tracer in Table III, encouraging the use of our model in future searches of local-type PNG in DESI data.

While we show results for a specific HOD parametrization suitable for DESI galaxies, this work shows great

promise for reducing the uncertainty on b_ϕ more broadly. Further studies are warranted to extend our results to more general galaxy populations, and comparing our results with similar analyses using hydrodynamical simulations and semi-analytical models will be very compelling [as done in e.g., 81].

We hope that future analyses of galaxy surveys can adopt Lagrangian-bias informed priors on the parameter b_ϕ , such as those presented in this work, and be able to constrain the local-type PNG parameter $f_{\text{NL}}^{\text{loc}}$ with less bias and smaller uncertainty.

ACKNOWLEDGMENTS

BH is supported by the Miller Institute for Basic Science. SF is supported by Lawrence Berkeley National Laboratory and the Director, Office of Science, Office of

High Energy Physics of the U.S. Department of Energy under Contract No. DE-AC02-05CH11231.

This research used resources of the National Energy Research Scientific Computing Center, which is supported by the Office of Science of the U.S. Department of Energy under Contract No. DE-AC02-05CH11231. Additional computations in this work were performed at facilities supported by the Scientific Computing Core at the Flatiron Institute, a division of the Simons Foundation.

DATA AVAILABILITY

The simulations used in this work are publicly available. Instructions for access and download are given at <https://abacussummit.readthedocs.io/en/latest/data-access.html>.

[1] N. Bartolo, E. Komatsu, S. Matarrese, and A. Riotto, *Phys. Rept.* **402**, 103 (2004).

[2] M. Alvarez *et al.*, arXiv e-prints arXiv:1412.4671 (2014).

[3] A. Achúcarro *et al.*, arXiv e-prints arXiv:2203.08128 (2022).

[4] E. Komatsu, D. N. Spergel, and B. D. Wandelt, *Astrophys. J.* **634**, 14 (2005).

[5] N. Dalal, O. Doré, D. Huterer, and A. Shirokov, *Phys. Rev. D* **77**, 123514 (2008).

[6] Planck Collaboration *et al.*, *A&A* **641**, A9 (2020).

[7] R. de Putter and O. Doré, *Phys. Rev. D* **95**, 123513 (2017).

[8] N. Sailer, E. Castorina, S. Ferraro, and M. White, *JCAP* **12**, 049 (2021).

[9] M. Schmittfull and U. Seljak, *Phys. Rev. D* **97**, 123540 (2018).

[10] U. Giri, M. Münchmeyer, and K. M. Smith, *Phys. Rev. D* **107**, L061301 (2023).

[11] A. Moradinezhad Dizgah *et al.*, *J. Cosmology Astropart. Phys.* **2021**, 015 (2021).

[12] L. R. Abramo, J. V. D. Ferri, and I. L. Tashiro, *J. Cosmology Astropart. Phys.* **2022**, 013 (2022).

[13] S. Jolicoeur, R. Maartens, and S. Dlamini, *European Physical Journal C* **83**, 320 (2023).

[14] K. N. Abazajian *et al.*, arXiv e-prints arXiv:1610.02743 (2016).

[15] P. Ade *et al.*, *J. Cosmology Astropart. Phys.* **2019**, 056 (2019).

[16] U. Seljak, *Phys. Rev. Lett.* **102**, 021302 (2009).

[17] P. McDonald and U. Seljak, *J. Cosmology Astropart. Phys.* **2009**, 007 (2009).

[18] G. M. Bernstein and Y.-C. Cai, *MNRAS* **416**, 3009 (2011).

[19] S. Ferraro and K. M. Smith, *Phys. Rev. D* **91**, 043506 (2015).

[20] O. Darwish *et al.*, *Phys. Rev. D* **104**, 123520 (2021).

[21] T. Mergulhão, H. Rubira, R. Voivodic, and L. R. Abramo, *J. Cosmology Astropart. Phys.* **2022**, 021 (2022).

[22] Y. Wang *et al.*, *MNRAS* **498**, 3470 (2020).

[23] Y. Wang and G.-B. Zhao, *Research in Astronomy and Astrophysics* **20**, 158 (2020).

[24] A. Slosar *et al.*, *J. Cosmology Astropart. Phys.* **2008**, 031 (2008).

[25] B. Leistedt, H. V. Peiris, and N. Roth, *Phys. Rev. Lett.* **113**, 221301 (2014).

[26] E.-M. Mueller *et al.*, arXiv e-prints arXiv:2106.13725 (2021).

[27] E. Castorina *et al.*, *J. Cosmology Astropart. Phys.* **2019**, 010 (2019).

[28] G. Cabass *et al.*, *Phys. Rev. D* **106**, 043506 (2022).

[29] G. D’Amico, M. Lewandowski, L. Senatore, and P. Zhang, arXiv e-prints arXiv:2201.11518 (2022).

[30] A. Barreira *et al.*, *J. Cosmology Astropart. Phys.* **2020**, 013 (2020).

[31] T. Lazeyras, A. Barreira, F. Schmidt, and V. Desjacques, *J. Cosmology Astropart. Phys.* **2023**, 023 (2023).

[32] A. Barreira, *J. Cosmology Astropart. Phys.* **2022**, 013 (2022).

[33] V. Desjacques, U. Seljak, and I. T. Iliev, *MNRAS* **396**, 85 (2009).

[34] C. Wagner, L. Verde, and L. Boubekeur, *J. Cosmology Astropart. Phys.* **2010**, 022 (2010).

[35] W. R. Coulton *et al.*, *ApJ* **943**, 64 (2023).

[36] W. R. Coulton *et al.*, *ApJ* **943**, 178 (2023).

[37] E. Fondi *et al.*, *J. Cosmology Astropart. Phys.* **2024**, 048 (2024).

[38] A. Gutiérrez Adame *et al.*, *A&A* **689**, A69 (2024).

[39] A. Barreira, *J. Cosmology Astropart. Phys.* **2020**, 031 (2020).

[40] A. Barreira, *J. Cosmology Astropart. Phys.* **2022**, 033 (2022).

[41] B. Hadzhiyska, L. H. Garrison, D. J. Eisenstein, and S. Ferraro, *Phys. Rev. D* **109**, 103530 (2024).

[42] T. Tatekawa, arXiv e-prints astro (2004).

[43] N. A. Maksimova *et al.*, *MNRAS* **508**, 4017 (2021).

[44] L. H. Garrison, D. J. Eisenstein, and P. A. Pinto, *MNRAS* **485**, 3370 (2019).

[45] L. H. Garrison *et al.*, *MNRAS* **508**, 575 (2021).

[46] B. Hadzhiyska *et al.*, *MNRAS* **509**, 501 (2022).

- [47] J. F. Navarro, C. S. Frenk, and S. D. M. White, *ApJ***490**, 493 (1997).
- [48] R. H. Wechsler *et al.*, *ApJ***568**, 52 (2002).
- [49] A. D. Ludlow *et al.*, *MNRAS***441**, 378 (2014).
- [50] A. D. Ludlow *et al.*, *MNRAS***460**, 1214 (2016).
- [51] K. Wang *et al.*, *MNRAS***498**, 4450 (2020).
- [52] J. S. Bullock *et al.*, *MNRAS***321**, 559 (2001).
- [53] B. Diemer and A. V. Kravtsov, *ApJ***799**, 108 (2015).
- [54] A. A. Dutton and A. V. Macciò, *MNRAS***441**, 3359 (2014).
- [55] Y.-Y. Mao, A. R. Zentner, and R. H. Wechsler, *MNRAS***474**, 5143 (2018).
- [56] S. Yuan *et al.*, *MNRAS***502**, 3582 (2021).
- [57] G. L. Bryan and M. L. Norman, *ApJ***495**, 80 (1998).
- [58] U. Abbas and R. K. Sheth, *MNRAS***378**, 641 (2007).
- [59] A. Pujol, K. Hoffmann, N. Jiménez, and E. Gaztañaga, *A&A***598**, A103 (2017).
- [60] A. Paranjape, O. Hahn, and R. K. Sheth, *MNRAS***476**, 5442 (2018).
- [61] J. Shi and R. K. Sheth, *MNRAS***473**, 2486 (2018).
- [62] B. Hadzhiyska *et al.*, *MNRAS***493**, 5506 (2020).
- [63] N. Kaiser, *ApJ***284**, L9 (1984).
- [64] J. M. Bardeen, J. R. Bond, N. Kaiser, and A. S. Szalay, *ApJ***304**, 15 (1986).
- [65] F. Bernardeau, S. Colombi, E. Gaztañaga, and R. Scoccimarro, *Phys. Rep.***367**, 1 (2002).
- [66] V. Desjacques, D. Jeong, and F. Schmidt, *Phys. Rep.***733**, 1 (2018).
- [67] S. Dodelson and F. Schmidt, *Modern Cosmology* (PUBLISHER, ADDRESS, 2020).
- [68] Z. Vlah, M. White, and A. Aviles, *J. Cosmology Astropart. Phys.***2015**, 014 (2015).
- [69] R. A. Porto, L. Senatore, and M. Zaldarriaga, *J. Cosmology Astropart. Phys.***2014**, 022 (2014).
- [70] P. McDonald and A. Roy, *J. Cosmology Astropart. Phys.***2009**, 020 (2009).
- [71] L. Senatore, *J. Cosmology Astropart. Phys.***2015**, 007 (2015).
- [72] V. Assassi, D. Baumann, D. Green, and M. Zaldarriaga, *J. Cosmology Astropart. Phys.***2014**, 056 (2014).
- [73] Z. Vlah, E. Castorina, and M. White, *J. Cosmology Astropart. Phys.***2016**, 007 (2016).
- [74] T. Matsubara, *Phys. Rev. D***77**, 063530 (2008).
- [75] S. Yuan *et al.*, *MNRAS***530**, 947 (2024).
- [76] Z. Zheng *et al.*, *ApJ***633**, 791 (2005).
- [77] S. Yuan *et al.*, arXiv e-prints arXiv:2306.06314 (2023).
- [78] H. Guo *et al.*, *MNRAS***446**, 578 (2015).
- [79] S. Yuan *et al.*, *MNRAS***510**, 3301 (2022).
- [80] B. Hadzhiyska *et al.*, *MNRAS***508**, 698 (2021).
- [81] M. Shiferaw, N. Kokron, and R. H. Wechsler, (2024).